Florida State University Libraries

Simulated Signals for Highly Charged Heavy Stable Charged Particles

Justin Marquez

THE FLORIDA STATE UNIVERSITY

COLLEGE OF ARTS & SCIENCES

SIMULATED SIGNALS OF HIGHLY

CHARGED HEAVY STABLE

CHARGED PARTICLES

By

JUSTIN MARQUEZ

A Thesis submitted to the
Department of Physics
in partial fulfillment of the requirements for graduation with
Honors in the Major

Degree Awarded:
Spring, 2021

The members of the Defense Committee approve the thesis of Justin Marquez defended on April 6, 2021.

Dr. Todd Adams
Thesis Director

Dr. Arash Fahim
Outside Committee Member

Dr. Jorge Piekarewicz
Committee Member

Signatures are on file with the Honors Program office.

Contents

Abstract

The purpose of this thesis was to study new techniques to search for highly charged heavy stable charged particles (HSCPs) using simulation of the proton-proton interaction at the Compact Muon Solenoid detector at the Large Hadron Collider at CERN. These searches took place in the muon system using a modified Drell-Yan process and in the electromagnetic calorimeter (ECAL) using particle gun production. We found that the number of muons per event had dropped to a value too low to be useful well before $q = 16e$, confirming that the muon system was not a viable candidate for searches for highly charged HSCPs. For slow-moving HSCPs in the ECAL, we determined that the reconstructed time could be effectively used to identify HSCP signals. For an HSCP with transverse momentum $p_T = 200\,\text{GeV}/c$ and mass $m = 300\,\text{GeV}/c^2$, there was a significant shift of about $3\,\text{ns}$. This demonstrated the feasibility of the reconstructed time in HSCP identification.

List of Figures

List of Tables

1 Introduction

The study of particle physics helps us answer fundamental questions about the universe and the interactions that take place therein. The Standard Model (SM) of particle physics, which serves as a basis for this research, has passed numerous tests through various experimentation at particle colliders around the world, including at the Large Hadron Collider (LHC) at CERN. However, there are certain aspects of what we have observed that are not yet described by the SM. For example, we are still uncertain how to classify dark matter, dark energy, or gravitation. These gaps in the model have led to the creation of theories known as beyond the Standard Model (BSM), with a prominent example being supersymmetry (SUSY) [1].

This thesis will study the signals created by singly and multiply charged Heavy Stable Charged Particles (HSCPs). In previous searches by Compact Muon Solenoid (CMS) experiment [2], charges were studied in the range $e/3 < |q| < 8e$, where $e \approx 1.602 \times 10^{-19}$ C is the elementary charge, using the inner tracker and muon system. However, the efficiency in reconstructing muons for the higher charges dropped, inhibiting further searches. The ATLAS experiment, however, has been able to push the upper bound in electric charge to $|q| = 60e$ [3] and later to $|q| = 100e$ [4].

For this study, simulation [5] of the CMS detector system at the LHC was used to study signals generated by these particles for various charges. The purpose of this research is to study the simulated signals of HSCPs within the CMS detector and aid future searches for HSCPs from experimental data. We hope to address possible limitations of using reconstructed muons as a method to observe HSCP signals and explore the electromagnetic calorimeter (ECAL) as a more suitable approach to observe highly charged multiply charged HSCPs.

This thesis will first explore the SM and SUSY within this chapter. Chapter 2 will

focus on the experimental apparatus, the coordinate systems used, and the relevant effects of charged particles traveling through matter. Chapter 3 will discuss the simulation and all relevant parameters. Chapter 4 will describe the resultant data from the muon system and the electromagnetic calorimeter. Chapter 5 will summarize this thesis' findings and its significance.

1.1 The Standard Model

The SM describes three of the four fundamental forces and categorizes all known elementary particles into families of quarks, leptons, and force carriers. A figure depicting the current SM in full can be seen in Fig. 1. The three fundamental forces described in this model are the electromagnetic, strong, and weak forces. These three interactions have force carriers, which are particles that mediate their respective force. The photon mediates the electromagnetic force, gluons mediate the strong force, and weak bosons (Z^0, W^+, W^-) mediate the weak force. As discussed before, gravity is not present in the SM. The SM also includes the Higgs boson, the particle responsible for providing elementary particles with mass.

Each of the elementary particles has many quantum numbers, including electric charge, strong charge (color), and weak charge (isospin). The SM provides blueprints for particle interactions, which allow for the creation of the CMS software (CMSSW) used to simulate the proton-proton interactions. This is because protons are, in accordance with the model, made up of two up quarks and a down quark, and it is the elementary particles within the protons that collide.

All particles also satisfy the relation

$$E^2 = \mathbf{p}^2 c^2 + (mc^2)^2,\tag{1}$$

Standard Model of Elementary Particles
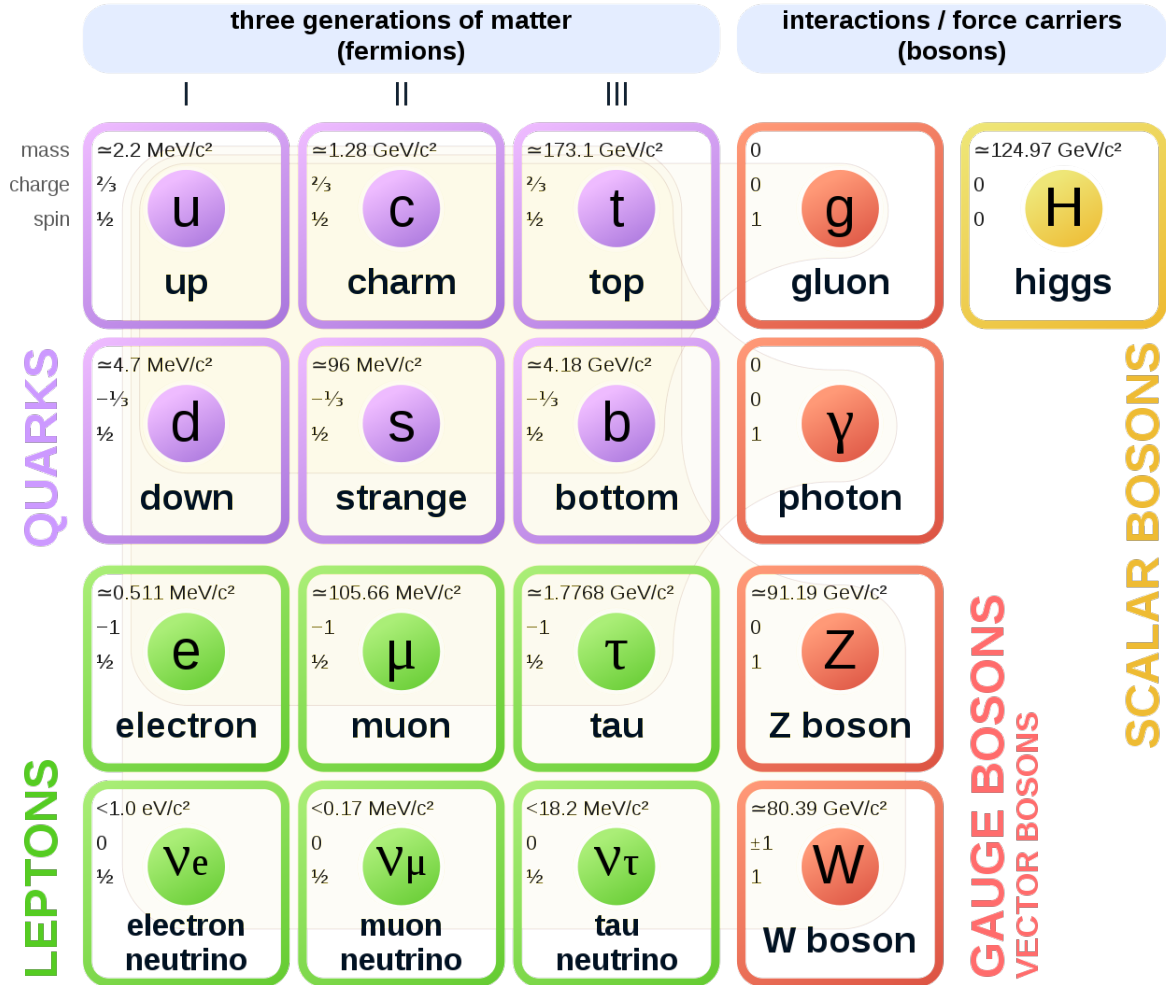
Figure 1: Diagram of the Standard Model of elementary particles. The first three columns demonstrate the three generations of matter, split up into two quarks and two leptons each. The last two columns demonstrate the force carriers for three of the four fundamental forces as well as the Higgs boson, responsible for providing mass to the elementary particles [6].

where E is the total energy of the particle, $\mathbf{p}$ is the vector representing the particle's momentum, m is the mass of the particle, and $c \approx 3 \times 10^8\,\mathrm{m\,s^{-1}}$ is the speed of light. Thus, any particle at rest has some intrinsic energy. This is why the LHC is attempting to achieve a proton-proton interaction with as much energy as possible; higher energies allow for the creation of more massive particles. As the first generation of particles is already well-observed, making up all ordinary matter [7], we hope to observe the more massive particles in the other generations and any allowed combinations therein.

1.2   Supersymmetry

However, as discussed previously, the SM cannot explain all theoretical particles, such as dark matter. For this reason, BSM theories have been formed and tested in an effort to expand the SM. SUSY is one of the leading theories within BSM and proposes that every elementary particle has a superpartner: a particle differing in spin by $\hbar/2$. It is inferred by experiment that these superpartners must be much more massive than SM particles, since they have not been detected to this day from experimentation. Figure 2 displays the SM alongside the proposed extension from SUSY.

Many extensions of SUSY allow for the possibility of a very massive, long-lived, charged particle. Here, long-lived is relative as the particle can have a lifetime of a few nanoseconds and still traverse a distance in the detector comparable to SM particles [9]. These are referred to as HSCPs and are the subject of study in this thesis. For this thesis, the HSCP mass will be considered at $300\,\mathrm{GeV}/c^2$, and can have a velocity $\beta \equiv v/c < 0.9$ as a result [9]. Thus, by looking for a larger time-of-flight measurement, HSCPs can be identified within experimental data. There are three broad categories for the HSCPs, relative to its charge Q: fractionally charged ($|Q| < 1e$), singly charged ($|Q| = 1e$), and multiply charged ($|Q| > 1e$).

SUSY allows for the creation of singly charged HSCPs, but there are theories that lead to the possibility of multiply charged HSCPs that can also be considered. Through SUSY, it
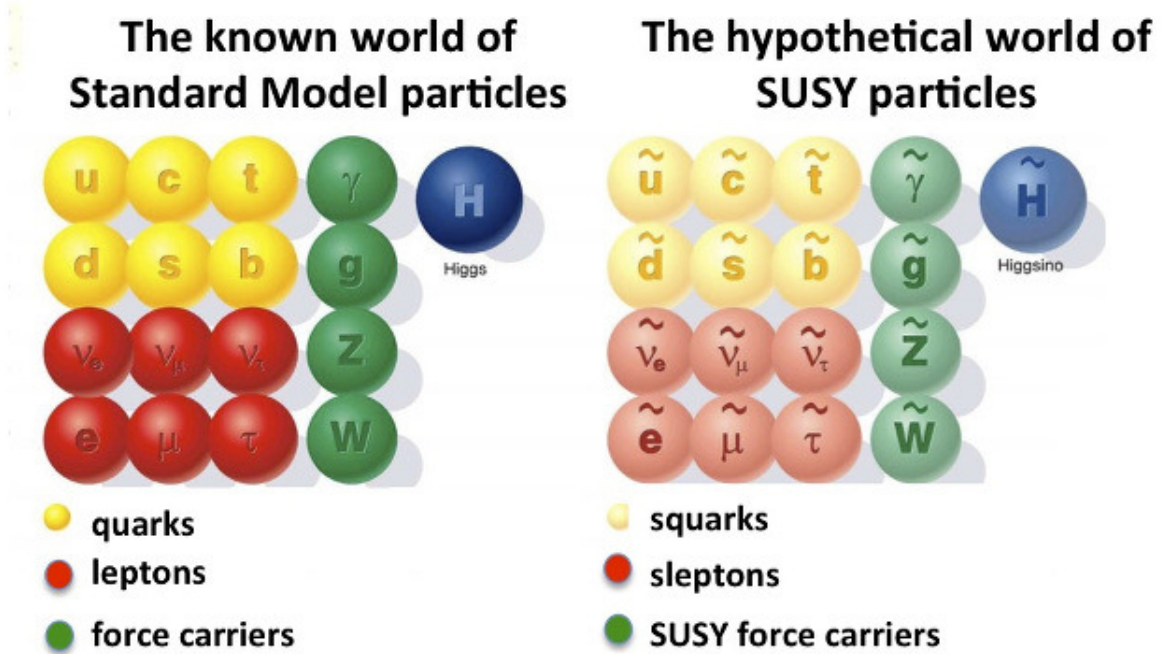
Figure 2: Diagram of the Standard Model of elementary particles (left) beside the supersymmetric extension (right) [8].

is possible for bound states of sorts to be created [10]. These bound states include numerous baryonic or leptonic balls called Q-balls [11]. If the Q-balls are sufficiently long-lived, they can be considered as multiply charged HSCP candidates. Otherwise, it is still possible for them to decay into possible long-lived candidates. As Q-ball charges have a maximum on the order of $Q_{\mathrm{max}} \sim 10^{34} e$, Q-balls could still be highly charged HSCP candidates [12]. While there is no experimental evidence of Q-balls yet, this thesis will explore new ways to search for evidence in LHC data. For the purposes of this study, however, it will not be assumed that the candidates we are studying are Q-balls.

2   Large Hadron Collider at CERN

The Large Hadron Collider (LHC) at CERN is a superconducting accelerator and collider with each of its proton beams reaching approximately 7 TeV, for a total center-of-mass collision energy of $\sqrt{s} \approx 14$ TeV. Its high-luminosity experiments, ATLAS and CMS, both reach a peak instantaneous luminosity of $L \approx 32\,\mathrm{cm}^{-2}\,\mathrm{s}^{-1}$ [13]. In general, higher luminosity implies more interactions occurring within the experiments, allowing for more data to be taken in a given time frame. The LHC is approximately 26.7 km in circumference and uses alternating electric fields to accelerate the proton beams. Once the protons have been accelerated into the ring structure of the LHC, magnetic fields are used to bend the proton beams. These beams only intersect at specific interaction points, where detectors are in place to record the results of collisions. This thesis will study signals for HSCPs within the CMS experiment, located at one of the interaction points of the LHC.

2.1   Compact Muon Solenoid Detector

The CMS detector system, displayed in Fig. 3, consists of many subdetectors: the (inner) silicon tracker, the electromagnetic calorimeter (ECAL), the hadronic calorimeter (HCAL), and the muon system. The CMS detector also includes a superconducting solenoid that provides a magnetic field $B = 4\,\mathrm{T}$ parallel to the beamline at the interaction point [14], inducing a curved path in the transverse direction for charged particles produced at the interaction point. This allows the algorithms that analyze the data to calculate the ratio of the particle's transverse momentum, or the component of the momentum perpendicular to the beamline p_T, to its electric charge q, as the radius of curvature R due to an external magnetic field B is given by

$$R = \frac{p_T}{qB}. \tag{2}$$

The direction the particle curves gives the sign of the electric charge, but we are still only able to determine the ratio p_T/q. It is also important to note that the superconducting solenoid encompasses only the inner tracker, ECAL, and HCAL detectors. Then, the magnetic field is in the opposite direction outside of the solenoid, resulting in a curved path in the opposite direction after particles have passed through it. Additionally, this assumes nonzero charge, since neutral particles will not experience a magnetic force. Furthermore, this is the classical case of curvature due to a magnetic field. However, it is a sufficient approximation because of the slow-moving nature of HSCPs. For the relativistic case, there is a multiplicative factor of γ, the Lorentz factor, given by

$$\gamma \equiv \frac{1}{\sqrt{1 - (v/c)^2}},$$

where $c = 3 \times 10^8 \, \mathrm{m\,s^{-1}}$ is the speed of light. For slow-moving particles, this factor is negligible since $\gamma(v \ll c) \approx 1$.

2.1.1 Relevant Coordinate System

For the purpose of this thesis, it is important to introduce the coordinate systems used by convention for the CMS experiment. The origin is at the nominal collision point at the center of the detector. The x-axis is pointed radially inward towards the center of the LHC, the y-axis is pointed vertically upward, and the z-axis is pointed to satisfy the relation $\hat{\mathbf{x}} \cdot \hat{\mathbf{y}} = \hat{\mathbf{z}}$. The azimuthal angle ϕ is measured from the $+x$-axis and the polar angle θ is measured from the $+z$-axis. As this experiment involves the interaction of relativistic particles, the experiment usually measures the polar angle using a variable called pseudorapidity η, given by $\eta \equiv \ln\tan(\theta/2)$ [14]. This variable is used in favor of the polar angle θ because for any given range of pseudorapidity $\Delta\eta$, there is approximately the same number of particles detected in that region. This makes pseudorapidity more favorable when making theoretical

CMS DETECTOR

Total weight : 14,000 tonnes
Overall diameter : 15.0 m
Overall length : 28.7 m
Magnetic field : 3.8 T

STEEL RETURN YOKE
12,500 tonnes

SILICON TRACKERS
Pixel (100x150 μm) ~16m² ~66M channels
Microstrips (80x180 μm) ~200m² ~9.6M channels

SUPERCONDUCTING SOLENOID
Niobium titanium coil carrying ~18,000A

MUON CHAMBERS
Barrel: 250 Drift Tube, 480 Resistive Plate Chambers
Endcaps: 468 Cathode Strip, 432 Resistive Plate Chambers

PRESHOWER
Silicon strips ~16m² ~137,000 channels

FORWARD CALORIMETER
Steel + Quartz fibres ~2,000 Channels

CRYSTAL ELECTROMAGNETIC CALORIMETER (ECAL)
~76,000 scintillating PbWO₄ crystals

HADRON CALORIMETER (HCAL)
Brass + Plastic scintillator ~7,000 channels

Figure 3: Diagram of the Compact Muon Solenoid detector system, demonstrating each of the detectors and their layout with respect to the beamline. This thesis focuses on the muon chambers (the outermost detectors) and the crystal electromagnetic calorimeter [15].

calculations and has consequently persisted in data analysis.

In simulation analysis, it is important to determine a method to identify a hit in the detector with the particle that was created by the proton-proton interaction. To do this, we must compare the position of the hit in the detector and the initial values of pseudorapidity η and azimuthal angle ϕ of the generated particles. Taking the curvature of the particles' trajectories due to the magnetic field, these positions must be fairly similar. So, we define

$$\Delta\phi \equiv \phi_{\text{hit}} - \phi_{\text{gen}}$$

and

$$\Delta\eta \equiv \eta_{\text{hit}} - \eta_{\text{gen}},$$

where the subscript "hit" refers to the reconstructed hit in the detector and "gen" refers to the generated particle. To match a hit with a generated particle, we then hope to minimize

$$\Delta R = \sqrt{(\Delta\phi)^2 + (\Delta\eta)^2}, \tag{3}$$

where ΔR is the displacement in $\eta - \phi$ space. The magnetic field would alter the azimuthal angle ϕ of the particle, since the field is parallel to the beamline. However, the polar angle θ and the pseudorapidity η would remain unchanged. To account for this, a correction term must be added to the generated azimuthal angle to approximate the effects of the magnetic field. The correction term is given by

$$\phi' = \sin^{-1}\left(\frac{qBR_{\text{E}}}{p_T}\right), \tag{4}$$

where q is the charge of the particle, B is the magnetic field strength, and p_T is the transverse momentum of the particle. The distance R_{E} is given by the radius of the inner face of the

ECAL plus the length of a single crystal, or $R_{\mathrm{E}} \approx 1.29 \,\mathrm{m} + 0.23 \,\mathrm{m}$. With this correction, Eqn. (3) becomes, in full,

$$\Delta R = \sqrt{\left(\Delta\phi - \sin^{-1}\left(\frac{qBR_{\mathrm{E}}}{p_T}\right)\right)^2 + (\Delta\eta)^2}. \tag{5}$$

By iterating over the reconstructed particles and minimizing this equation, we are able to identify particles in the detector for simulation analysis.

2.1.2 Electromagnetic Calorimeter

The ECAL encompasses the inner silicon tracker and is made up of 61 200 lead tungstate ($PbWO_4$) crystals in the central barrel and 7324 crystals on each endcap of the detector [14]. These scintillating crystals emit light with intensity proportional to the deposited energy, allowing photodetectors to record signals and calculate the energy deposited into the crystals by incoming particles. These photodetectors record the light bursts as functions of time, giving an idea of the timing between light emissions. The central barrel of the ECAL can detect particles in a pseudorapidity range of $|\eta| < 1.479$, while the endcaps cover $1.479 < |\eta| < 3.0$. The distance from the beamline to the inner face of the ECAL is about $1.29 \,\mathrm{m}$, and the length of each crystal is about $230 \,\mathrm{mm}$ [14]. The ECAL is designed to reconstruct the energy and time of electrons and photons. The reconstructed time of the particle is the arrival time at the ECAL compared to a particle traveling at the speed of light originated at the collision point. However, the ECAL is also able to detect ionization due to charged particles, such as HSCPs. More information on the reconstruction of time can be found in Ref. [16].

2.1.3 Muon System

The muon system is the outermost detector system of CMS, covering a total pseudo-rapidity range of $|\eta| < 2.4$, equivalent to a range of about $10° < \theta < 170°$ for the polar angle θ [14]. The muon system is one of the primary detectors of interest in CMS and is comprised of barrel drift tube (DT) chambers covering $|\eta| < 1.2$ and cathode strip chambers (CSC) covering $0.9 < |\eta| < 2.4$, giving a redundant range of $0.9 < |\eta| < 1.2$ [14].

The DTs are in a region with a low muon-rate and are situated such that they are able to accurately measure the radius of curvature of the charged particles and its momentum in the z-direction. The DTs are long tubes with a thin wire in the center filled with 85% Ar and 15% CO_2. The DTs are able to reconstruct the particle's path by measuring the time ionized gas particles within the chambers arrive at the wire. Knowing the time it would take for the ionized particles to hit the wire, the distance from the wire through which the particle passed is calculated. However, the distance from the wire gives an entire range of possible points of interaction. For this reason, several DTs are lined up next to each other in a staggered fashion to be able to determine the precise location of the particle by comparing hits in a cluster of DTs [14]. The CSCs are located in the endcaps, a region with a high muon-rate. The chambers are comprised of 6 anode wire planes interleaved among 7 cathode panels [14]. They are able to measure the azimuthal angle ϕ of the particle based on the induced charge on the plates.

Due to the uncertainty in background rates and other factors making it difficult to detect muons with accuracy, a separate detector system called the resistive plate chambers (RPC) were introduced, covering a pseudorapidity range of $|\eta| < 1.6$. The function of the RPCs is to provide an extra trigger with a high transverse momentum threshold, helping to reduce any uncertainties in the data.

3 Simulation

This section describes the stages of simulation and the two methods of particle production used in this thesis. Additionally, the varied parameters and chosen cutoff energies will be explained and derived.

3.1 CMS Software

There are several stages involved with the interaction simulation in CMSSW. The flow of data for the CMS detector can be seen in Fig. 4. First, the generator stage simulates the proton-proton interaction by creating the resultant particles and their energy-momentum four-vectors. For the studies completed for this thesis, the Pythia 6.4 generator was used [17]. The CMSSW detector simulation stage simulates the interactions of the particles with the detector using a toolkit called GEANT [18], which essentially creates a three-dimensional replica of the detector system in the code. The simulation increments the position of the particles in accordance with its energy-momentum four-vector and deposits energy appropriately in the different segments of the detector system.

The CMSSW digitization stage converts the energy deposits into electronic signals, such as those recorded by the CMS detectors. For instance, the ECAL does not actually measure the energy deposited into the crystals, but rather measures the intensity of the light emitted by scintillation within the crystals using photodetectors and calculates the deposited energy this way. The same process will be modeled by the software.

The CMSSW simulates the trigger decisions on the electronic signals created by the digitization stage using the Level 1 Trigger and the High Level Trigger. These triggers are different, but both set certain criteria that must be met for the signals to be saved to disk and not simply discarded. This is done because the proton-proton interaction generates so many particles each second that some events must be discarded as unimportant in comparison

Figure 4: Figure of the flow of simulated and experimental data for the CMS detector. This figure demonstrates the different stages of interaction simulation, as well as all of the necessary subprocesses and extra steps required to complete the simulation. The figure shows the order of stages for interaction simulation: generation, detector simulation, digitization, level 1 trigger simulation, digitization to raw data (digi2raw), High Level Trigger, and reconstruction [19].

to the rest in a search for new or interesting phenomena. Before the High Level Trigger, CMSSW converts the electronic signals recorded into data in the same form as experimental data, allowing it to be analyzed using the same methods.

The CMSSW reconstruction stage, which is the primary focus of study in this thesis, is not unique to interaction simulation; this stage is used for experimental data as well. This process interpolates trajectories of the particles based on the information given by signals in the detector systems and values calculated from those signals. This step can be done for both simulated and experimental data, as getting approximate trajectories is an important part of both options. This is possible because the last portion of the digitization process, called "digi2raw" in Fig. 4, converts simulated data into the proper format for reconstruction. The trajectories are created within detectors, such as within crystal clusters in the ECAL, as well as between different detectors. An example of reconstruction between multiple detectors are

global muons, which are particles that have reconstructed trajectories in the muon system and other detectors.

Another important process of CMSSW is pileup simulation. About every 25 ns, a bunch crossing occurs in which a proton bunch collides with another proton bunch. This results in multiple proton-proton interactions taking place for each bunch crossing. In an attempt to mimic this effect, CMSSW adds additional standard interactions on top of the specific event being simulated, which results in generally uninteresting noise that must be dealt with during analysis. This process takes place before digitization, as can be seen in Fig. 4.

3.1.1 Particle Generation

The Drell-Yan [20] (DY) process is the process in which a quark and antiquark pair from interacting hadrons annihilate and create a lepton pair. For the purposes of this thesis, a modified DY process was used that generated a pair of fourth-generation leptons τ'. To model the relatively long-lived nature of the HSCP, the τ' particle is prohibited from decaying and an additional decay of the Z boson was implemented. Specifically,

$$Z \longrightarrow \tau' + \bar{\tau}'.$$

Particle gun production is much simpler. This process simply generates the desired particle at the interaction point and assigns its properties based on the configuration file. For this thesis, the `FlatRandomPtGunProducer` was used, which allowed for the input of a range of values for transverse momentum p_T, pseudorapidity η, and azimuthal angle ϕ. The energy of the particle would consequently be calculated from the given transverse momentum and particle mass. This method has the capability of producing an antiparticle with the desired particle, but this option was unused for this study. This process does not model the proton-proton interaction and cannot be compared with experimental data but is nonetheless

interesting due to the possibility of studying HSCPs with little to no noise.

3.2   Cutoffs and Parameters

For analysis of the reconstructed signals in the ECAL, it was necessary to determine appropriate methods of isolating HSCP signals from the simulated pileup and general noise. To isolate the HSCP signals, we decided to implement a cutoff value for the energy deposited into each crystal in the ECAL. If the reconstructed energy for a given crystal (also referred to as a hit) did not meet this threshold, that signal was discarded. An appropriate cutoff energy was determined that significantly reduced noise while preserving as many signals due to HSCPs as possible. To determine this cutoff, it is important to know what can be discarded as noise. Figure 5 demonstrates the energy deposited per crystal in the ECAL barrel for a charge $q = 50e$. In the far left of the figure, there is a wide peak corresponding to pileup and general noise. The noise can be suppressed by employing a cutoff at about $0.6\,\mathrm{GeV}$, but this would compromise HSCP signal for lower charges, as seen in Fig. 6. To avoid these complications, a less strict cutoff of about $0.3\,\mathrm{GeV}$ was employed to preserve as much HSCP signal as possible.

To evaluate the efficiency of the chosen energy cutoff, the total energy deposited into the ECAL per event for 1000 events was plotted for the detector simulation stage as well as the reconstruction stage as seen in Figs. 7 and 8. An effective cutoff energy would imply a reconstructed energy distribution similar to its generated counterpart. Once the pileup is mostly suppressed, the only signal left should be that due to the HSCPs, thus approximating the generated distribution. As seen in Fig. 7, the distribution corresponding to the reconstruction stage has the same form as that corresponding to the detector simulation stage. The only two differences are the horizontal shift by about $+50\,\mathrm{GeV}$ and the new peak at about $50\,\mathrm{GeV}$. These differences occur because all of the noise and simulated pileup is depositing large amounts of energy into the detector, making it difficult to isolate the HSCP

16

Figure 5: Distribution of the energy deposited into the ECAL barrel per hit displayed as a semi-log plot for particle gun production with charge $q = 50e$ and transverse momentum $p_T = 1000\,\mathrm{GeV}/c$.
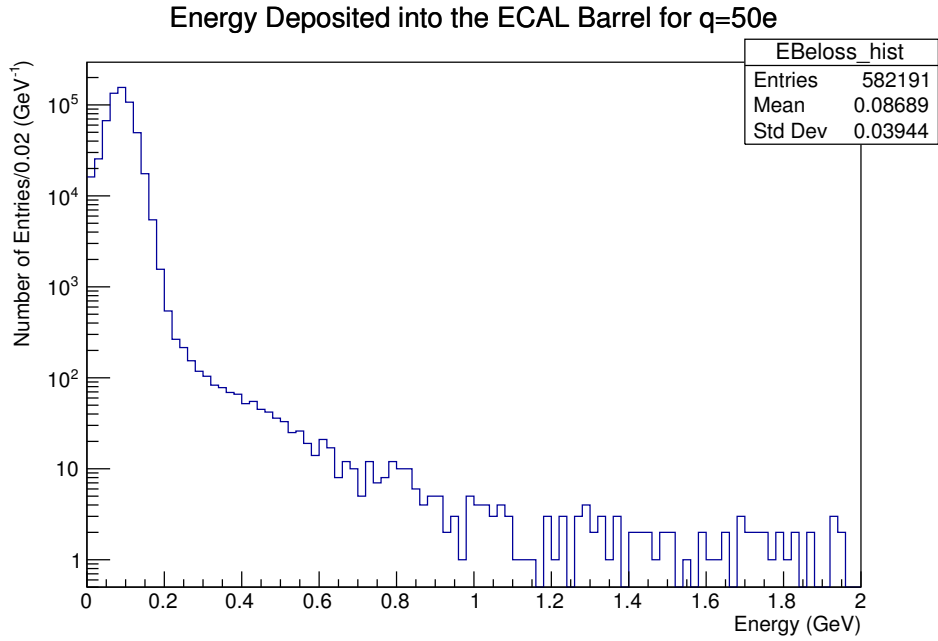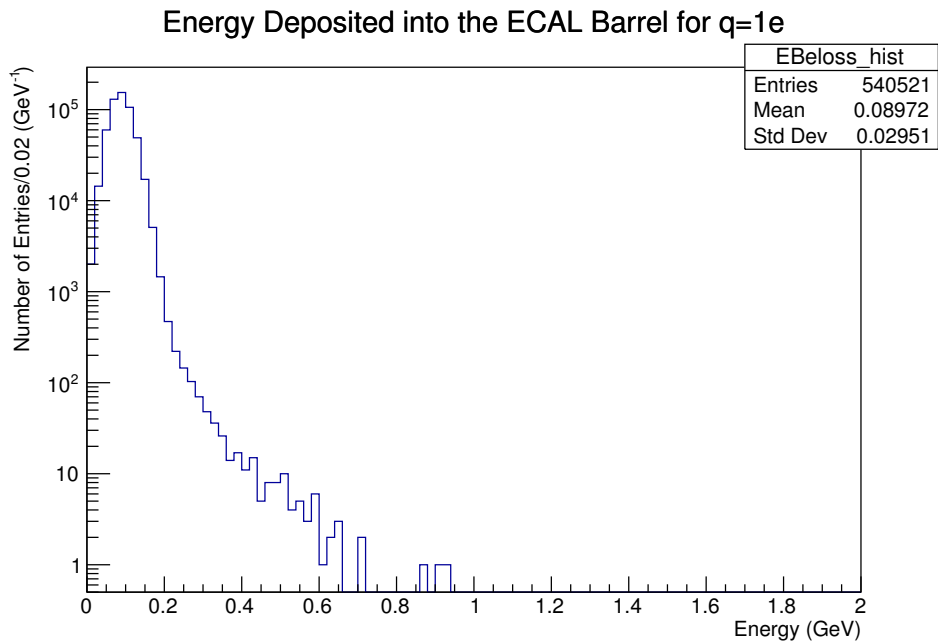

Figure 6: Distribution of the energy deposited into the ECAL barrel per hit displayed as a semi-log plot for particle gun production with charge $q = e$ and transverse momentum $p_T = 1000\,\mathrm{GeV}/c$.

signal. The cutoff was successful in reducing significant noise and restoring the original energy distribution for the detector simulation stage, as can be seen in Fig. 8.

For this thesis, the mass of the generated HSCPs was fixed at $m = 300\,\text{GeV}/c^2$ for both DY and particle gun production. For both methods of particle production, 1000 events were generated. The conditions of the 2016-2018 dataset (Run 2) were used in the simulation using CMSSW 7.4.14.

Table 1: Table of all parameters and their values for DY particle production. Charge is the only varied parameter for this method.

Variable	Values
Number of Events	1000
Charge q (e)	3, 4, 5, 6, 8, 10, 12, 16, 20, 22, 23
Mass m (GeV/c^2)	300

Table 2: Table of all parameters and their values for particle gun production. As there is much more freedom in this method, all relevant information for the position and momenta of the particle were specified. The energy of the particle is determined by their pseudorapidity and transverse momentum.

Variable	Values
Number of Events	1000
Charge q (e)	1, 3, 4, 5, 6, 8, 10, 12, 16, 20, 22, 34, 50
Mass m (GeV/c^2)	300
Transverse momentum p_T (GeV/c)	200, 300, 400, 600, 1000
Pseudorapidity η	[-2.1, 2.1]
Azimuthal Angle ϕ	$[-\pi, \pi]$

Figure 7: Distribution of total energy deposited into the ECAL barrel per event for the detector simulation stage (blue) and reconstruction stage (red) for particle gun production with charge $q = 50e$ and transverse momentum $p_T = 1000\,\mathrm{GeV}/c$.
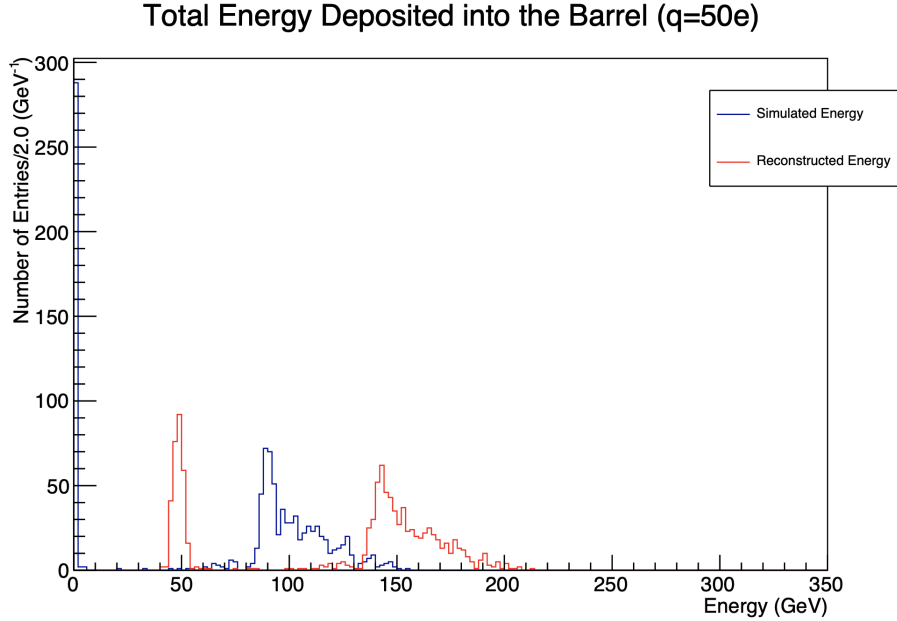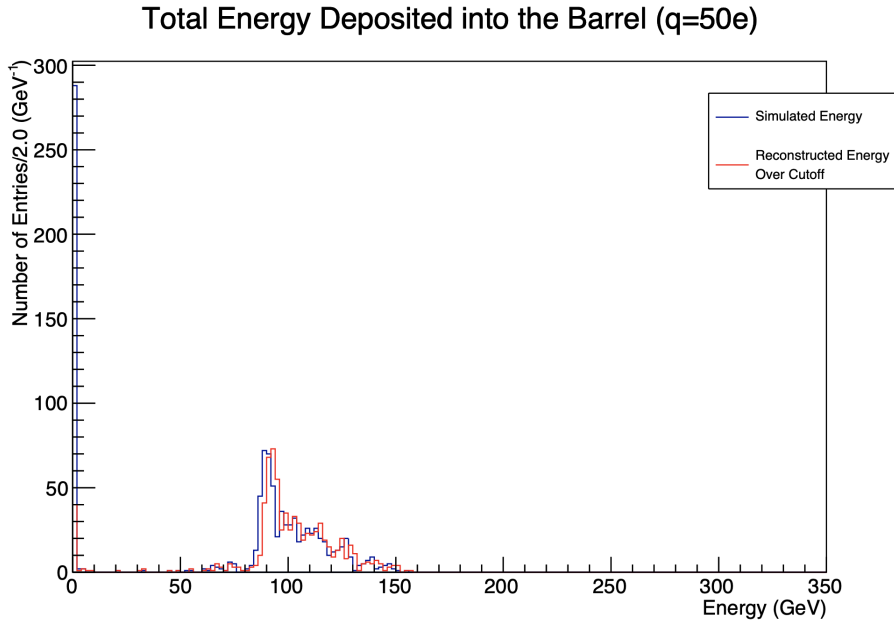

Figure 8: Distribution of total energy deposited into the ECAL barrel per event for the detector simulation stage (blue) and reconstruction stage (red) for particle gun production with charge $q = 50e$ and transverse momentum $p_T = 1000\,\mathrm{GeV}/c$. For the reconstructed distribution, only hits with deposited energy exceeding $0.3\,\mathrm{GeV}$ were counted.

19

4   Results and Analysis

For this thesis, HSCP signals were analyzed within the muon system and the electromagnetic calorimeter with a fixed mass of $300\,\mathrm{GeV}/c^2$ and discrete values of charge $q \in [1e, 100e]$. For the analysis of the muon system, DY production was used to achieve a better understanding of how HSCP signals may compare to data being observed experimentally at CMS. For analysis of the ECAL, particle gun production was used. This will not be seen experimentally but is nonetheless useful to study to give insight into the exact signals generated by the HSCPs. Each run simulated 1000 events for both methods of HSCP production.

4.1   Muon System

For the DY process, HSCPs with charges $3e < |q| < 23e$ were generated. Figure 9 demonstrates the number of reconstructed muons detected per event in the muon system as a function of charge. This histogram only counted reconstructed muons with a transverse momentum of $p_T > 55\,\mathrm{GeV}/c$. This cutoff value was chosen to match the trigger for Run 2. In experiment, the particles that would reach the muon system are almost always muons and, for this reason, any particle that can have a path interpolated within the muon system during the reconstruction stage is considered a reconstructed muon. Since HSCPs can make it to the muon system, they will be reconstructed as muons and must be isolated using the appropriate cutoff mentioned above. It is important to note that in DY production, used for this analysis, the HSCP and its antiparticle will be produced. At most, we expect two reconstructed muons per event corresponding to the HSCP and its antiparticle. However, it is not certain that the HSCPs will reach the muon system, so we see slightly fewer for lower charges in Fig. 9.

Similar to past analysis of multiply charged HSCPs in the muon system [21], the efficiency of the muon system dropped rapidly as charge increased. The number of muons per event

had dropped to a value too low to be useful well before $q = 16e$ and, consequently, dropped significantly in efficiency of reconstructing an HSCP in the muon system. This implies that the muon system is a poor choice for studying highly charged HSCPs.
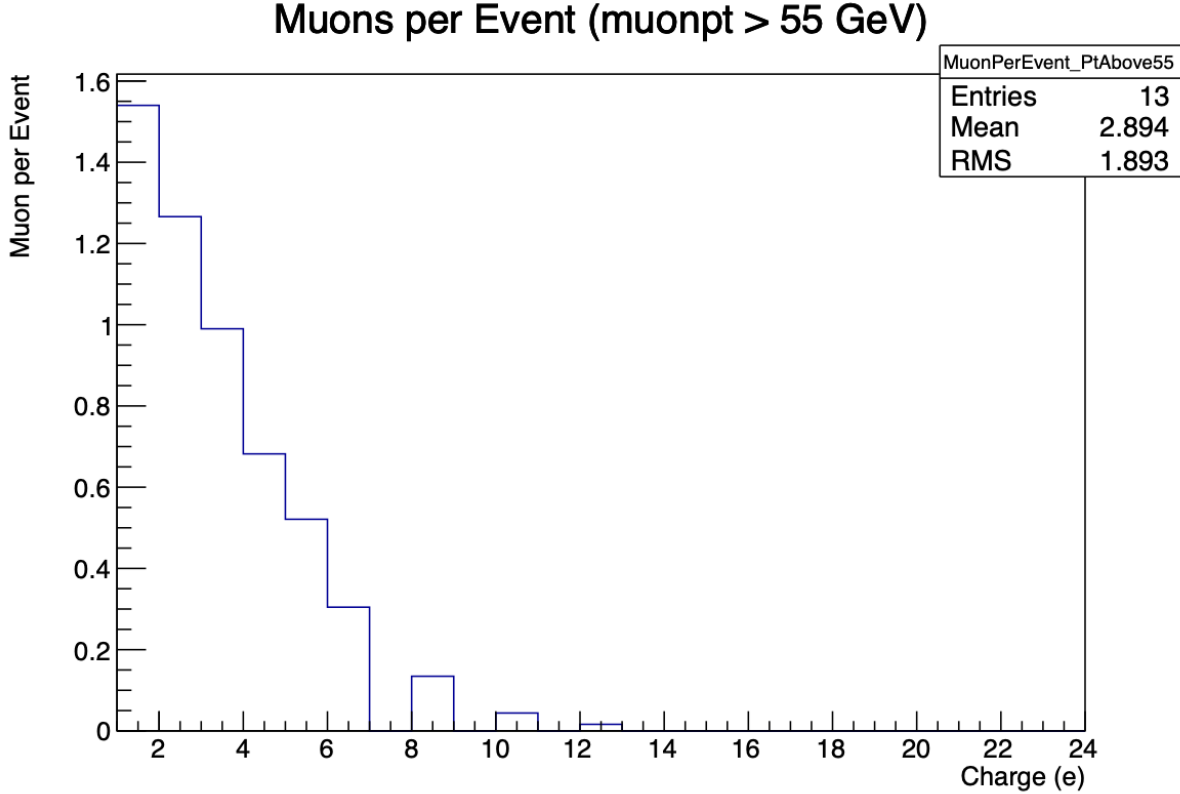
Figure 9: Distribution of the number of reconstructed muons detected per event as a function of HSCP charge for DY production with charges $3e < |q| < 23e$ and mass $m = 300\,\mathrm{GeV}/c^2$.

The effect seen in Fig. 9 can be explained by observing the reconstructed transverse momentum calculated as a function of charge for these results. As seen in Fig. 10, the transverse momentum decreases as the charge of the HSCP increases. The primary reason for this effect is due to the assumptions made by the CMSSW software. The assumption is that the reconstructed muons are singly charged particles. By looking at Eqn. (2), we see that

$$p_T = qBR,$$

21

where B and R are both measurable quantities for the detector. With the assumption $q = 1e$, we see that the detector will calculate a transverse momentum $p'_T = BR$. The radius of curvature R is given by Eqn. (2), giving a final result of

$$p'_T = \frac{p_T}{q},$$

where p_T is the true transverse momentum of the particle. As seen in the equation above, as the charge increases the transverse momentum calculated by the reconstruction stage decreases and deviates from the true value. So, for higher charges, this effect would lower transverse momentum measurements and make detection of multiply charged HSCPs in the muon system difficult.

It is possible that this effect is partly as a result of energy loss when traveling through matter, as given by the Bethe formula. For a charged particle with charge qe with speed βc traveling through material with proton number Z and nucleon number A, the Bethe formula is given by

$$\left\langle -\frac{\mathrm{d}E}{\mathrm{d}x} \right\rangle = Kq^2 \frac{Z}{A} \frac{1}{\beta^2} \left[\frac{1}{2} \ln \frac{2m_e c^2 \beta^2 \gamma^2 W_{\max}}{I^2} - \beta^2 - \frac{\delta(\beta\gamma)}{2} \right], \tag{6}$$

where $W_{\max}$ is the maximum possible energy transfer in a collision, m_e is the mass of an electron, c is the speed of light, γ is the Lorentz factor, $\delta(\gamma\beta)$ is a density-effect correction function, and I is the mean excitation potential of the material. This formula is valid in the region $0.1 \lesssim \beta\gamma \lesssim 1000$ with an accuracy of a few percent [22]. The relationship that is important in this study, however, is the relation to the particle's charge, given by

$$\left\langle -\frac{\mathrm{d}E}{\mathrm{d}x} \right\rangle \propto q^2.$$

So, as the charge of the HSCP increases, we expect more energy loss as it travels through the detectors. Since the particle's mass does not change, the change happens in the particle's

Mean muonpt vs. Charge

QvsMuonPt	
Entries	13
Mean	4.742
RMS	4.567
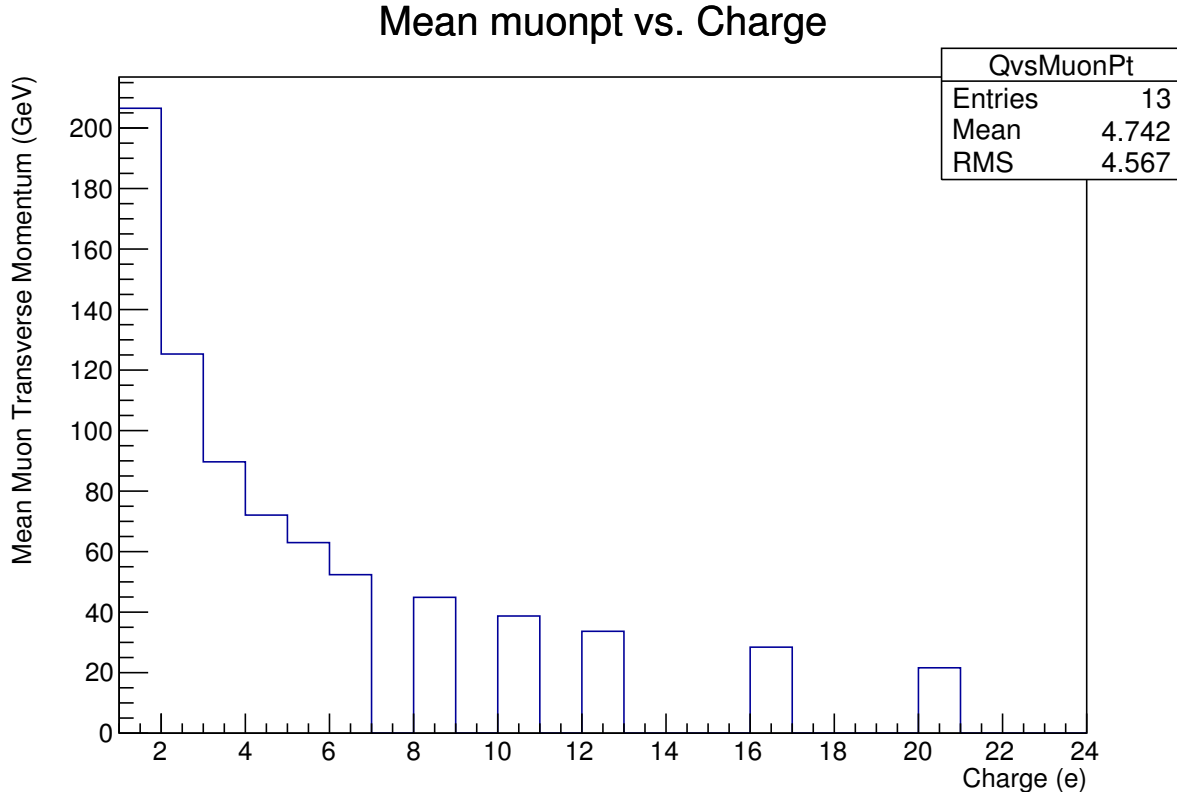
Figure 10: Distribution of the mean transverse momentum of reconstructed muons as a function of HSCP charge for DY production with charges $3e < |q| < 23e$ and mass $m = 300\,\mathrm{GeV}/c^2$.

momentum, as seen by the relation in Eqn. (1). Due to the rapid decline in efficiency for highly charged HSCPs, HSCP signals in the ECAL were studied. In the ECAL, the singly-charged assumption's effect on the simulation is negligible.

4.2 Electromagnetic Calorimeter

If the highly charged HSCPs are truly stopping before reaching the muon system due to the effects of the Bethe formula in Eqn. (6), then looking at a detector closer to the beamline should alleviate this problem. If the loss in detection efficiency is due to the singly-charged assumption, then it is similarly useful to search for HSCPs at a detector that is effectively unaffected by the assumption. In either case, observing signals within the ECAL

would ensure the detection of highly charged HSCPs. In fact, we expect to see more energy deposited in the ECAL for highly charged HSCPs compared to lower charges due to the Bethe formula.

However, the proximity of the ECAL to the beamline also implies that there will be significant activity in the detector due to electrons, photons, and other particles passing through the detector at the same time. For this reason, the ECAL was analyzed using particle gun production in CMSSW instead of DY production. The muon system did not have these concerns since most particles would have been stopped due to energy loss before reaching it. Even though a simple matching algorithm was derived in Eqns. (3) and (4), the particle gun production was chosen to avoid errors due to possible mismatching. By shooting one particle into the detector system, it is trivial to isolate the signals that it produces in the detector system. Using the particle gun, appropriate cutoff energies were determined in Sec. 3.2.

To confirm the accuracy of the simple matching algorithm in Eqn. (5), the displacement ΔR was plotted for the reconstructed hit that deposited the most energy in that event in the ECAL barrel and the generated particle. The reconstructed hits were chosen by the maximum deposited energy as this would likely correlate to the HSCP signal. This distribution can be seen in Fig. 11, demonstrating relatively small values that have mostly trailed off by about $\Delta R \approx 0.07$. This leads to the conclusion that this simple matching algorithm is effective in identifying HSCP signals with relatively low noise.

As discussed previously, HSCPs will be relatively slow due to their high mass. For this reason, we hope to analyze the reconstructed time as registered by the ECAL to be able to identify the HSCPs. For this portion of the study, the transverse momentum of the HSCP was varied, taking values of $p_T \in \{200\,\text{GeV}/c, 300\,\text{GeV}/c, 400\,\text{GeV}/c, 600\,\text{GeV}/c, 1000\,\text{GeV}/c\}$. Figure 12 displays the distributions of reconstructed time in the ECAL barrel for these values of transverse momenta. For these plots, the appropriate energy cutoffs were used

ΔR at Maximum Energy Deposited into the ECAL

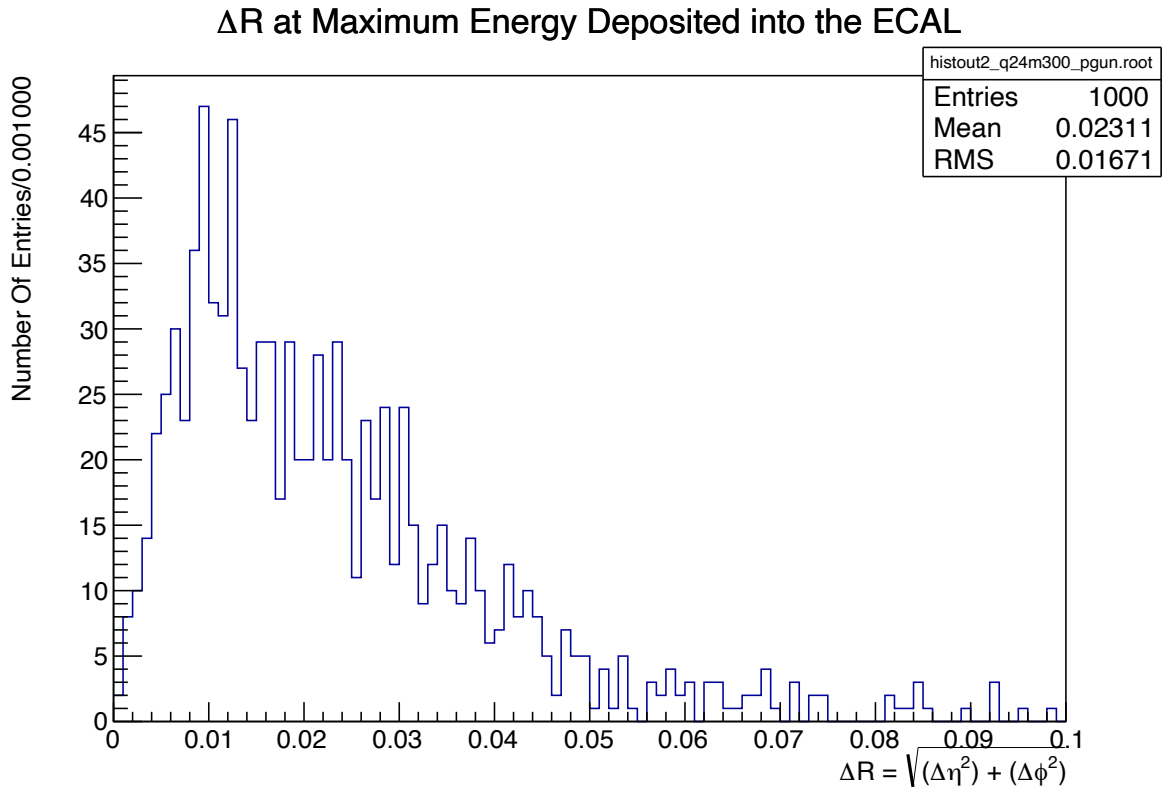| histout2_q24m300_pgun.root	
Entries	1000
Mean	0.02311
RMS	0.01671

Figure 11: Distribution of displacement ΔR in $\eta - \phi$ space between the generated particle and the reconstructed hit with maximum deposited energy for particle production with charge $q = 8e$ and transverse momentum $p_T = 1000 \, \text{GeV}/c$.

as described in Sec. 3.2. Additionally, only entries that had valid time and error values were considered, as provided by the member functions `EcalRecHit::isTimeValid()` and `EcalRecHit::isTimeErrorValid()`. Invalid values can occur from issues when fitting the reconstructed time with expected distributions. As expected, HSCPs with high transverse momentum are speed-of-light particles and have corresponding reconstructed times values near zero. These particles will be difficult to identify in simulated data produced by the DY process and in experimental data, so it is favorable to study HSCPs with lower transverse momentum.

The averages of the distributions in Fig. 12 are plotted in Fig. 13 for easy comparison. From these figures, it is apparent that as transverse momentum increases the efficiency in detecting HSCPs through reconstructed timing decreases.

Since it is easier to identify slow-moving HSCPs with reconstructed timing, we will study distributions for various charges with transverse momentum $p_T = 200\,\text{GeV}/c$. From Figs. 12 and 13, it can be seen that the slow-moving nature of HSCPs can be used to identify them in the ECAL up to about $p_T = 300\,\text{GeV}/c$ for HSCPs of mass $m = 300\,\text{GeV}/c^2$. In general, we assume that this trend would imply that the timing provides a relatively detectable shift in reconstructed timing for

$$p_T c \lessapprox mc^2.$$

To understand how the reconstructed timing of the particle depends on the charge of the HSCP, the transverse momentum was fixed at $p_T = 200\,\text{GeV}/c$ and the charge was varied for $q \in \{5e, 10e, 22e, 34e\}$, as seen in Fig. 14. As the charge increases, the number of entries drastically decreases. The cause of this phenomenon is not yet understood, but it may possibly be due to the effects of the Bethe formula, Eqn. (6). Additionally, the low transverse momentum and high charge lead to a small radius of curvature, given by Eqn. (2). For high charges there is a much greater loss of energy per unit distance than for lower charges and
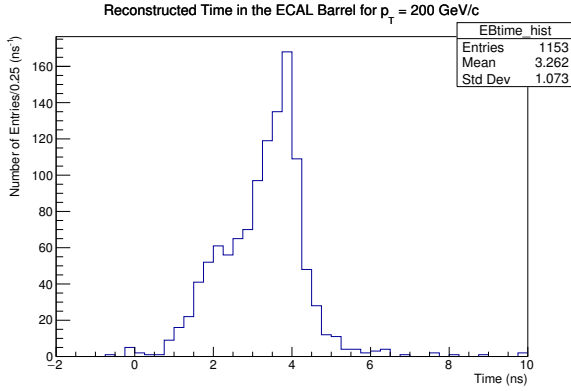
(a) Transverse momentum $p_T = 200\,\mathrm{GeV}/c$
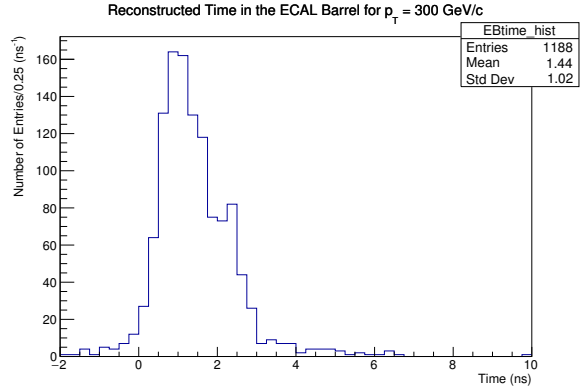
(b) Transverse momentum $p_T = 300\,\mathrm{GeV}/c$
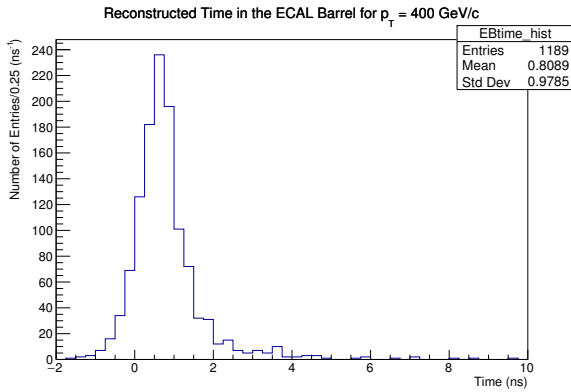
(c) Transverse momentum $p_T = 400\,\mathrm{GeV}/c$
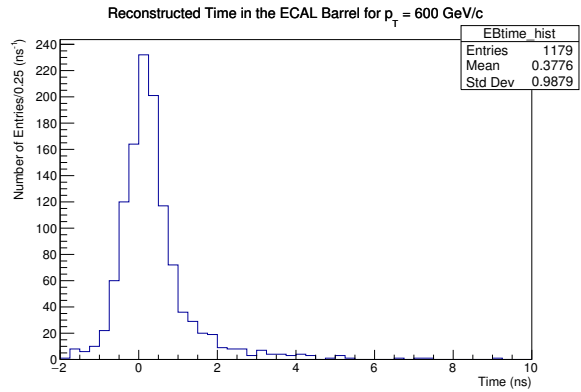
(d) Transverse momentum $p_T = 600\,\mathrm{GeV}/c$
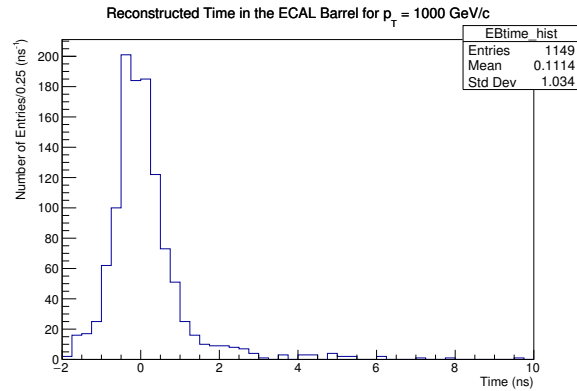
(e) Transverse momentum $p_T = 1000\,\mathrm{GeV}/c$

Figure 12: Distributions of reconstructed time in the ECAL barrel in the range $-2\,\mathrm{ns}$ to $10\,\mathrm{ns}$ for transverse momenta $p_T = 200\,\mathrm{GeV}/c$ (upper left), $p_T = 300\,\mathrm{GeV}/c$ (upper right), $p_T = 400\,\mathrm{GeV}/c$ (middle left), $p_T = 600\,\mathrm{GeV}/c$ (middle right), and $p_T = 1000\,\mathrm{GeV}/c$ (bottom) for particle gun production with charge $q = 5e$.

Figure 13: Distribution of the average reconstructed timing of an HSCP with charge $q = 5e$. The average was taken in the range $-2\,\mathrm{ns}$ to $10\,\mathrm{ns}$. These values are tabulated in Tab. 3.

this would results in a loss of transverse momentum and, consequently, a decreasing radius of curvature. It is possible that the loss of entries is due to the particles' inability to reach the ECAL, but this would require further study.

(a) Charge $q = 5e$

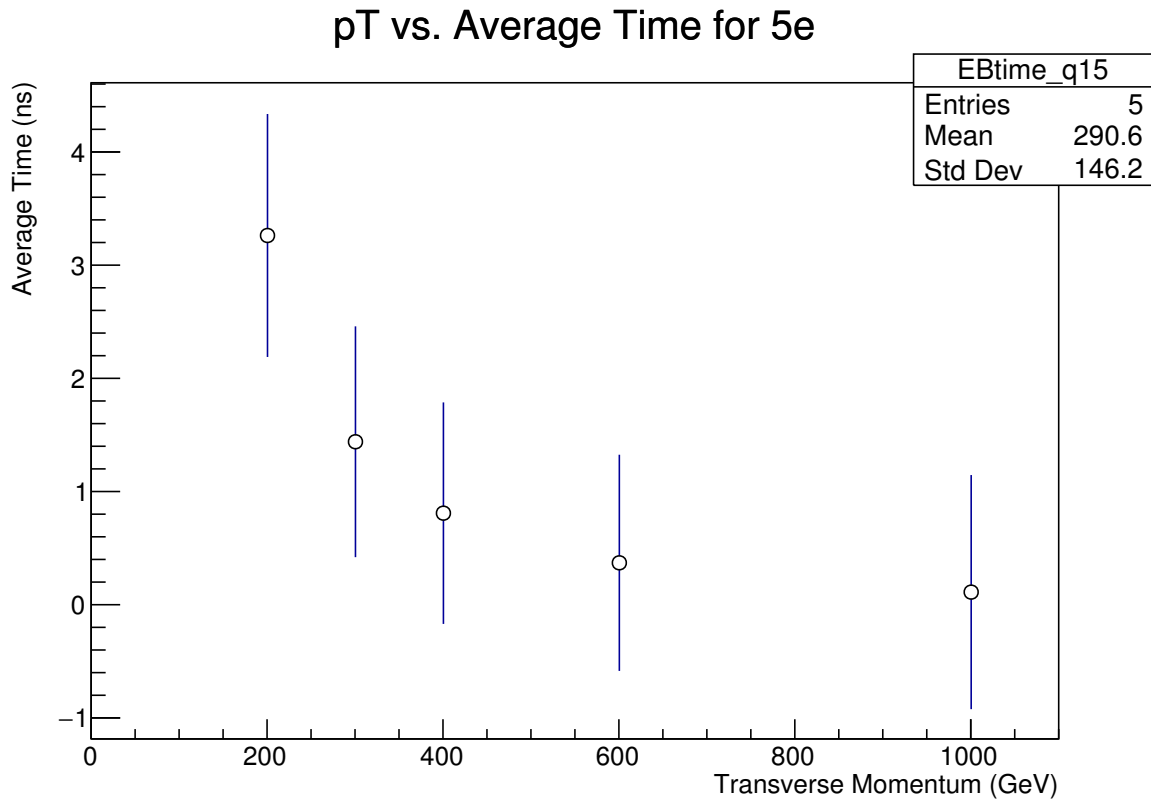(b) Charge $q = 10e$

(c) Charge $q = 22e$

(d) Charge $q = 34e$
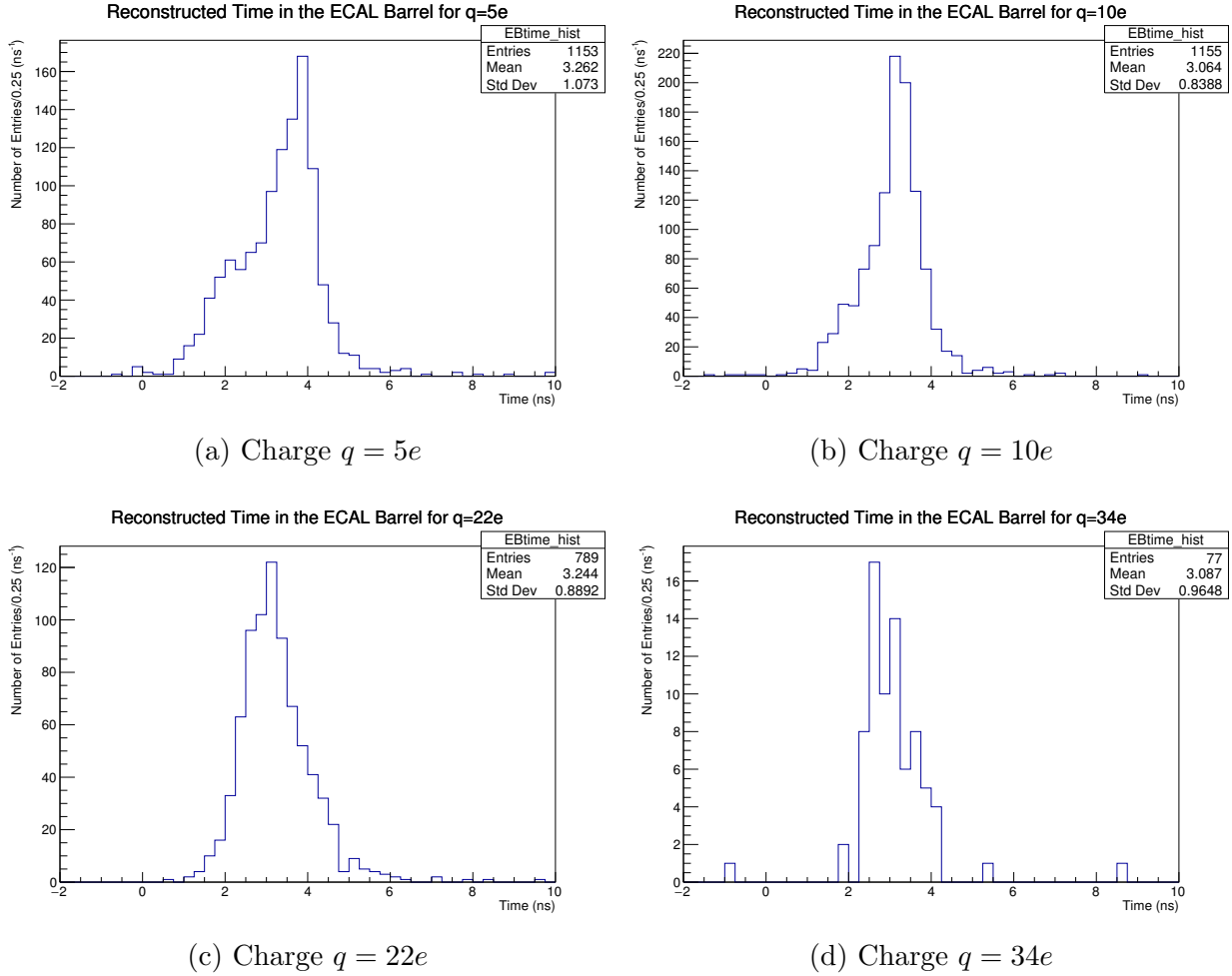
Figure 14: Distributions of reconstructed time in the ECAL barrel in the range $-2\,\mathrm{ns}$ to $10\,\mathrm{ns}$ for charges $q = 5e$ (upper left), $q = 10e$ (upper right), $q = 22e$ (lower left), and $q = 34e$ (lower right) for particle gun production with transverse momentum $p_T = 200\,\mathrm{GeV}/c$.

To see a general trend, the averages of the distributions in Fig. 14 were plotted against the charge, as seen in Fig. 15. However, for HSCPs with charge $q = 50e$, the average timing has already fallen near zero. While this seems to imply they are traveling faster than the particles with lower charges, this is entirely due to insufficient entries. In fact, there were

only 5 entries of valid reconstructed time above the cutoff energy of $0.6\,\mathrm{GeV}$ for the HSCP with charge $q = 50e$. Despite the problems due to the loss in entries, there is a relative shift in reconstructed timing at about $3\,\mathrm{ns}$ from that of speed-of-light particles. This demonstrates the feasibility of identifying low-momentum HSCPs using the reconstructed time.

Figure 15: Distribution of the average reconstructed timing of an HSCP with transverse momentum $p_T = 200\,\mathrm{GeV}/c$. The average was taken in the range $-2\,\mathrm{ns}$ to $10\,\mathrm{ns}$. These values are tabulated in Tab. 4.

Additionally, the average reconstructed time was plotted as a function of charge for varying values of transverse momentum, as seen in Fig. 16. The observed drop in efficiency takes place at higher charges for higher transverse momentum and cannot be observed by the highest momentum. However, by that point the timing is already near zero and is irrelevant to our studies. It can also be seen in the figure that as the transverse momentum increases, the average reconstructed time decreases as expected.

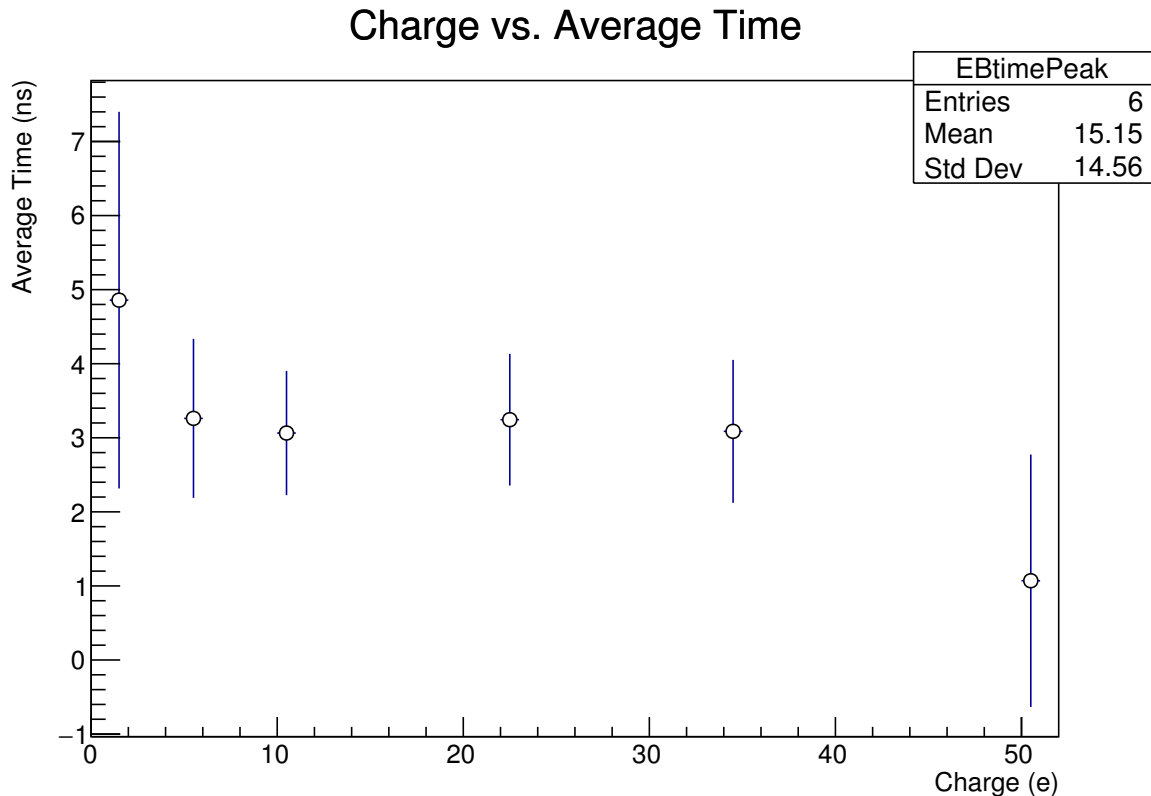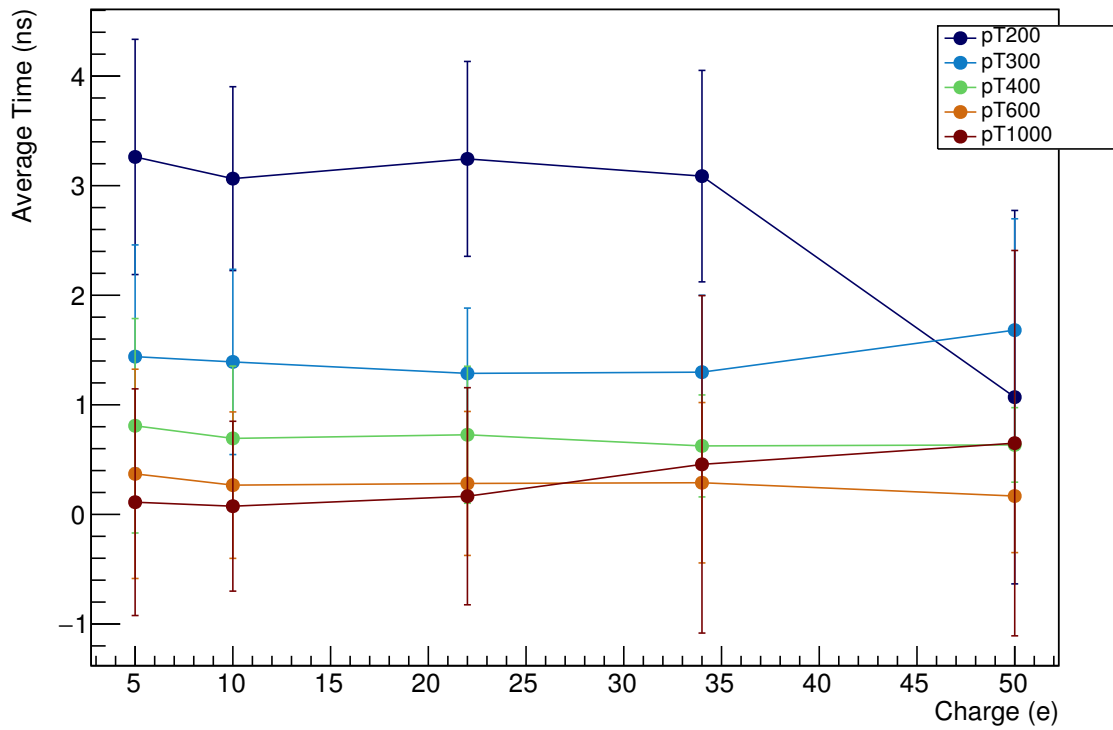Figure 16: Distribution of the average reconstructed timing of an HSCP with varying transverse momentum. The average was taken in the range $-2\,\mathrm{ns}$ to $10\,\mathrm{ns}$. These values are tabulated in Tab. 5.

The results displayed in Figs. 13 and 15 demonstrate the possibility of using the ECAL to identify highly charged HSCPs using reconstructed timing. Since previous CMS searches for HSCPs were primarily focused on the muon system [9, 21], it is promising to provide evidence of a technique that will facilitate searches for higher charges ($|q| > 8e$). While the muon system had significantly lower efficiency past $q = 8e$, Fig. 16 implies that much higher charges can be observed in the ECAL. However, there is the noticeable drop in efficiency found between charges $q \in [22e, 34e]$ for a transverse momentum of $p_T = 200\,\mathrm{GeV}/c$, indicating the need for further study. In general, the ECAL serves as a much better alternative for searching for highly charged HSCP signals.

5 Conclusions

We have studied the signals due to HSCPs within the CMS muon system and the CMS electromagnetic calorimeter using Drell-Yan production and particle gun production, respectively. By varying the charge in the DY process, it has been confirmed that the efficiency of reconstructing muons for HSCPs drops significantly as the charge increases. For this reason, the muon system is not a suitable candidate for searches for HSCPs with charge $|q| > 8e$. This problem arises from the singly-charged assumption made by the reconstruction code. As the charge increases, the reconstruction of the transverse momentum decreases, reducing the efficiency of this search.

An alternative technique was uncovered by studying signals induced by the HSCPs within the ECAL. In the ECAL, the effects due to the singly-charged assumption are negligible. In principle, HSCPs are slow-moving in nature, allowing for their identification using the reconstructed timing. The reconstructed time is measured relative to the time it would take a particle traveling at the speed of light to arrive at the crystal. Thus, slow-moving particles will have a nonzero peak in a reconstructed time distribution.

We have been able to confirm that this method is a viable option for identifying slow-moving highly charged HSCPs in the CMS experiment. The slow-moving condition has been estimated as $p_T c \lessapprox mc^2$, and has shown to be fairly accurate for a mass of $m = 300 \, \text{GeV}/c^2$. For HSCPs with transverse momentum $p_T = 200 \, \text{GeV}/c$, there was a shift of about $3 \, \text{ns}$ from zero, demonstrating the feasibility of this method to identify HSCPs.

There are various possible methods of continuing these studies. It is still unknown as to why the number of entries decreases as charge increases for reconstructed timing values. Further study can be done to identify the cause of this problem and rectify it to continue searches for highly charged HSCPs. Additionally, searches can be done in an effort to identify the upper bounds for transverse momentum and electric charge for efficient identification at

variable masses. These additions will provide insight to the efficiency of this new method for observing HSCPs in the CMS experiment.

A Tables

Table 3: Tabulated results of the average reconstructed timing of an HSCP with charge $q = 5e$. The average was taken in the range $-2\,\text{ns}$ to $10\,\text{ns}$. The distribution can be seen in Fig. 13.

p_T (GeV/c)	Average Timing (ns)	Uncertainty (ns)
200	3.26	1.07
300	1.44	1.02
400	0.81	0.98
600	0.37	0.95
1000	0.11	1.03

Table 4: Tabulated results of the average reconstructed timing of an HSCP with transverse momentum $p_T = 200\,\text{GeV}/c$. The average was taken in the range $-2\,\text{ns}$ to $10\,\text{ns}$. The distribution can be seen in Fig. 15.

q (e)	Average Timing (ns)	Uncertainty (ns)
1	4.86	2.54
5	3.26	1.07
10	3.06	0.84
22	3.24	0.89
34	3.09	0.96
50	1.07	1.70

Table 5: Tabulated results of the average reconstructed timing of an HSCP with varying transverse momentum. The average was taken in the range $-2\,\text{ns}$ to $10\,\text{ns}$. The distribution can be seen in Fig. 16.

p_T (GeV/c)	q (e)	Average Timing (ns)	Uncertainty (ns)
200	5	3.26	1.07
	10	3.06	0.84
	22	3.24	0.89
	34	3.09	0.96
	50	1.07	1.70
300	5	1.44	1.02
	10	1.39	0.85
	22	1.29	0.60
	34	1.30	0.70
	50	1.68	1.02
400	5	0.81	0.98
	10	0.69	0.66
	22	0.73	0.63
	34	0.62	0.47
	50	0.63	0.34
600	5	0.37	0.95
	10	0.27	0.67
	22	0.28	0.66
	34	0.29	0.73
	50	0.17	0.52
1000	5	0.11	1.03
	10	0.07	0.77
	22	0.17	0.99
	34	0.46	1.54
	50	0.65	1.76

References

[1]   Stephen P. Martin. "A Supersymmetry primer". In: *Adv. Ser. Direct. High Energy Phys.* 21 (2010). Ed. by Gordon L. Kane, pp. 1–153. DOI: `10.1142/9789812839657_0001`. arXiv: `hep-ph/9709356`.

[2]   S. Chatrchyan et al. "Searches for long-lived charged particles in pp collisions at $\sqrt{s}$=7 and 8 TeV". In: *Journal of High Energy Physics* 2013.7 (July 2013). ISSN: 1029-8479. DOI: `10.1007/jhep07(2013)122`. URL: `http://dx.doi.org/10.1007/JHEP07(2013)122`.

[3]   Georges Aad et al. "Search for magnetic monopoles and stable particles with high electric charges in 8 TeV *pp* collisions with the ATLAS detector". In: *Phys. Rev. D* 93.5 (2016), p. 052009. DOI: `10.1103/PhysRevD.93.052009`. arXiv: `1509.08059 [hep-ex]`.

[4]   Georges Aad et al. "Search for Magnetic Monopoles and Stable High-Electric-Charge Objects in 13 Tev Proton-Proton Collisions with the ATLAS Detector". In: *Phys. Rev. Lett.* 124.3 (2020), p. 031802. DOI: `10.1103/PhysRevLett.124.031802`. arXiv: `1905.10130 [hep-ex]`.

[5]   *CMS Software (CMSSW)*. Version 7.4.14. URL: `https://cmsdoxygen.web.cern.ch/cmsdoxygen/CMSSW_7_4_14/doc/html/index.html`.

[6]   *Standard Model of Elementary Particles*. Image. URL: `https://upload.wikimedia.org/wikipedia/commons/0/00/Standard_Model_of_Elementary_Particles.svg`.

[7]   T. P. Cheng and L. F. Li. *GAUGE THEORY OF ELEMENTARY PARTICLE PHYSICS*. 1984. ISBN: 978-0-19-851961-4.

[8]   *Table of the Standard Model (left) particles and their hypothetical supersymmetric particles.* URL: https://cdn.arstechnica.net/wp-content/uploads/2014/04/SM-SUSY-diagram.jpg.

[9]   *Search for Heavy Stable Charged Particles.* Tech. rep. CMS-PAS-EXO-11-022. Geneva: CERN, 2011. URL: http://cds.cern.ch/record/1370057.

[10]   Alexander Kusenko. "Solitons in the supersymmetric extensions of the standard model". In: *Phys. Lett. B* 405 (1997), p. 108. DOI: 10.1016/S0370-2693(97)00584-4. arXiv: hep-ph/9704273.

[11]   Sidney R. Coleman. "Q Balls". In: *Nucl. Phys. B* 262 (1985). [Erratum: Nucl.Phys.B 269, 744 (1986)], p. 263. DOI: 10.1016/0550-3213(86)90520-1.

[12]   Tuomas Multamaki and Iiro Vilja. "Limits on Q ball size due to gravity". In: *Phys. Lett. B* 542 (2002), pp. 137–146. DOI: 10.1016/S0370-2693(02)02274-8. arXiv: hep-ph/0205302.

[13]   Lyndon Evans and Philip Bryant. "LHC Machine". In: *Journal of Instrumentation* 3.08 (Aug. 2008), S08001–S08001. DOI: 10.1088/1748-0221/3/08/s08001. URL: https://doi.org/10.1088/1748-0221/3/08/s08001.

[14]   The CMS Collaboration et al. "The CMS experiment at the CERN LHC". In: *Journal of Instrumentation* 3.08 (Aug. 2008), S08004–S08004. DOI: 10.1088/1748-0221/3/08/s08004. URL: https://doi.org/10.1088/1748-0221/3/08/s08004.

[15]   *CMS Detector Diagram.* Image. URL: https://cmsexperiment.web.cern.ch/sites/cmsexperiment.web.cern.ch/files/cms_160312_02.png.

[16]   S Chatrchyan et al. "Time Reconstruction and Performance of the CMS Electromagnetic Calorimeter". In: *JINST* 5 (2010), T03011. DOI: 10.1088/1748-0221/5/03/T03011. arXiv: 0911.4044 [physics.ins-det].

[17] Torbjorn Sjostrand, Stephen Mrenna, and Peter Z. Skands. "PYTHIA 6.4 Physics and Manual". In: *JHEP* 05 (2006), p. 026. DOI: 10.1088/1126-6708/2006/05/026. arXiv: hep-ph/0603175.

[18] S. Agostinelli et al. "GEANT4–a simulation toolkit". In: *Nucl. Instrum. Meth. A* 506 (2003), pp. 250–303. DOI: 10.1016/S0168-9002(03)01368-8.

[19] *CMS Data-Flow Overview*. Image. URL: http://opendata.cern.ch/static/docs/cms-mc-production-overview/diagram.png.

[20] I. R. Kenyon. "The Drell-Yan Process". In: *Rept. Prog. Phys.* 45 (1982), p. 1261. DOI: 10.1088/0034-4885/45/11/002.

[21] Venkatesh Veeraraghavan. "Search for multiply charged Heavy Stable Charged Particles in data collected with the CMS detector." PhD thesis. Florida State U., 2013. DOI: 10.2172/1128814.

[22] *Review of Particle Physics*. 8th ed. Vol. 2020. Aug. 2020. Chap. 34, pp. 535–537. DOI: https://doi.org/10.1093/ptep/ptaa104.